Egy. J. Pure & Appl. Sci. 2022; 60(2):14-26

Egyptian Journal of Pure and Applied Science

Fabrication of zinc aluminate ($ZnAl_2O_4$) nanoparticles from solid industrial wastes

A. A. Abd-Allah [1], A. M. M. Amin [2], A, O. Youssef [1], Y. M. Z. Ahmed [2]

[1] *Chemistry Department, Faculty of Science, Ain Shams University, Abbassia, Cairo, Egypt.*
[2] *Refractory and Ceramic Materials Department, Central Metallurgical Research and Development Institute, CMRDI, Helwan 11421, Egypt.*

ARTICLE INFO

Received 08 April 2022
Accepted 16 May 2022

Keywords
Solid industrial waste,
Zinc aluminate nanoparticles,
Solid state,
Molten salt.

Correspondence
A. A. Abd-Allah

E-mail
asmaaabdelbaset_p@sci.asu.edu.eg
assmaaabdelbaset1989@gmail.com

ABSTRACT

The recovery of new materials from industrial waste is the target of many scientists and researchers all over the world. Zinc and aluminum sludge powders came from big iron and aluminum sheets industry were used as starting materials for zinc aluminate fabrication. The collected sludge powders were characterized by using XRF, XRD and DTA investigations, hydrozincite ($Zn_5(CO_3)_2(OH)_6$) and gibbsite ($Al(OH)_3$) are the main phases of zinc and aluminum sludges, respectively. Solid-state reaction (SSR) and molten salt synthesis (MSS) were carried out at 1100°C for 5 h by 3°C/min, using the collected sludge without any primary sophisticated chemical treatments. SSR and MSS samples were characterized by using XRD, FTIR, XPS, SEM and TEM investigations. Pure phase zinc aluminate nanoparticles were achieved by SSR and MSS with 17.4 and 12.7 nm, respectively. The microstructure of SSR sample was characterized by a high degree of particles aggregation, whereas the structure's homogeneity was modified by MSS. Optical properties of SSR and MSS samples were studied by using UV-visible and PL spectroscopy, the band gab energies were found to be 2.78 and 2.48 eV for SSR and MSS samples, respectively. MSS sample was distinguished by higher absorbance efficiency and lower recombination rate than SSR sample. The small band gab energy and the high absorbance efficiency evaluate this material for photocatalytic application as like as, organic dyes degradation in waste water treatments.

1. Introduction

Recently, researchers greatly try to direct their plans to use industrial wastes instead of commercial raw materials in the production of new materials. The recovery of new materials from industrial wastes added a big value to the new materials and seems to be environmentally friend and economically advantageous rout. Mainly, the supposed experimental rout must avoid the high cost and complicated procedure. In avoiding the drawbacks of literature researches represented in expensive materials and sophisticated instruments.

An important class of ceramic materials is the spinel type mixed metals oxides, including zinc aluminate ($ZnAl_2O_4$). The spinel structure of zinc aluminate was found in nature as a mineral named gahnite. It is a typical example of compounds of general formula (A)[B]O, where A and B are divalent and trivalent cations, respectively [1,2]. Zinc aluminate has excellent properties as like as, high chemical and thermal

stability, high mechanical resistance and low surface acidity [3,4]. These excellent properties promoted this kind of materials to be suitable for a wide range of applications as like as, refractory materials, optical coating for aerospace applications or host matrix. Zinc aluminate is suitable for ultraviolet (UV) photoelectronic application due to its wide band gab energy (3.2-3.9 eV) [5]. Recently, zinc aluminate has been largely used as photocatalyst in several reactions such as, photocatalytic degradation of organic dyes for waste water treatments [6,7]. Furthermore, zinc aluminate can be used as catalyst support in many organic transformations such as, paraffin dehydrogenation, saturated alcohols dehydration to olefins, methanol and heavy alcohols synthesis [2,8].

Owing to the great importance of zinc aluminate, several methods have been employed for its synthesis as like as, co-precipitation, combustion, sol-gel, hydrothermal, microwave hydrothermal and solid-state reaction (SSR) methods [5,9–12]. In solid-state reaction, the disadvantages represented in the inhomogeneity, lack of stoichiometry control, high temperature and low surface area [13]. However these, the solid-state reaction has many advantages, it is simple to perform; starting materials are often readily available at low cost. No solvents are needed in solid reactions and hence products don't require extensive purification to remove traces of solvent and impurities. The big novelty of the solid-state process is the high yield products, since; the products weight range can be from a few grams to several kilograms, so, it is economically preferred over several synthesis methods [10].

Current research in materials production is to avoid the disadvantages of SSR, such as the difficulty of nanosize and structure homogeneity achieving. For the modification of SSR, molten salt synthesis (MSS) could be utilized [14], in which, a salt of low melting point could be used as a dissolution medium for materials preparation from their solid constituents (oxides and carbonates). Salts as like as, KCl, NaCl, LiCl or a mixture of two salts could be used as a molten salt. Formally, reactants can be mixed with molten salt and the mixture heated above the melting temperature of the salt. The production of homogeneous nanosize particles depends on the ability of molten salt to dissolve all the reactant particles, and this depends on the ability of molten salt to act as a good medium for high mobility of liquid reactant particles. This enhances the rate of the solid-state reaction by increasing the contact area between the reactant particles, and the produced particles spontaneously precipitated from liquid phase. Whereas, the produced particles precipitated under supersaturation of dissolved reactants particles, nanosize could be easily produced. Molten salt synthesis promoted by desirable advantage, that molten salt doesn't react with neither the reactants nor the products, and can be easily removed by washing with distilled water. Therefore, the importance of molten salt can be concluded in increasing the reaction rate and achieving nanosize with homogenous structure [15].

This work interested in synthesizing zinc aluminate nanoparticles completely from industrial wastes through solid state reaction and molten salt synthesis. This can be discussed in the following statements: Recycling of the solid industrial wastes, which cause an air, water and soil pollution, and represent a very big load in get rid and transporting. Studying the ability to produce nanoparticles of zinc aluminate through the SSR and MSS. Carrying out chemical, structural, morphological and optical characterizations of the synthesized samples to evaluate the synthesized material for important application.

2. Materials and Methods

2.1 Industrial wastes collection

Industrial wastes represented in the aluminum and zinc sludge powders; aluminum sludge produced during the aluminum sheet production in ALUIMISR (aluminum manufacture company-Egypt). As well as, zinc sludge produced during the blast furnace operation for big iron production in Iron and Steel company-Egypt. During the iron extraction from its ore and its conversion into alloys, blast furnace sludge produced, it contains many elements impurities beside Fe and C. Of these impurities, Zn causes a significant problem: because it evaporates at lower temperature at the beginning of the metallurgical process and then condenses on the walls of the blast furnace. The condensed Zn generates dusts by large amounts, which may damage the furnace coating. Also, it prevents the furnace load (mixture of iron ores, additives, and cokes) to coming down, this leads to a sudden falling of the load. The blast furnace gets rid of the evaporated Zn by three routes; part of it leaves the furnace from

the gas flow and condenses on the dust particles, which normally removed in the air pollution control system. The smaller particles are washed out in a wet scrubber and generate sludge. While, large particles (>50 µm) are removed with the flue gas in a dust bag and a cyclone and can directly be recovered in the blast furnace after sintering [16]. The collected Zn and Al samples sludge were characterized by XRF, XRD and DTA analysis.

2.2 Synthesis of zinc aluminate by SSR and MSS

In solid state reaction, zinc and aluminum sludge powders were mixed by 1:2 molar ratio of Zn: Al, calculated according to the XRF given weight percentages of Zn and Al compounds in their sludge. Accurate grinding of the sludges' mixture is performed in presence of distilled water for 1 h at 300 rpm using a ball milling device. The grinded powder got out from the miller container and placed in a petri dish; the powder dried at 100°C overnight. Dried mixture powder was grinded using agate mortar, compressed as pellets with 5 gm, and heated in muffle furnace at 1100°C for 5 h by 3°C /min. The heated pellets got out from the furnace and grinded again in agate mortar, washed with warm distilled water then dried at 100°C for 1 h to be ready for the characterization.

In molten salt synthesis, potassium chloride (KCl) was added to the sludges' mixture by 4:1 of potassium chloride: zinc aluminate before the compression step and the mixture manually grinded very well.

2.3 Characterization of the collected sludges and the synthesized zinc aluminate samples

The collected industrial wastes and the synthesized zinc aluminate samples were characterized by X-ray diffraction (XRD, Bruker axis D8, Germany) with Cu-Kα (λ = 1.5406 Å) radiation and secondary mono-chromator in the range 2θ-scale from 4-70°. The crystallite size of the synthesized SSR and MSS samples was determined from the X-ray diffraction data using the Debye–Scherrer formula: $d_{RX} = K\lambda/ß\cos\theta$

Where d_{RX} is the crystallite size, K=0.9 is a correction factor to account for particle shapes. ß is the full width at half maximum (FWHM) of the mostintense diffraction peak, λ is the wave length of Cu target = 1.5406 °A, and θ is the Bragg angle. The chemical analysis of zinc and aluminum sludges were determined by XRF analyzer, model advanced Axios Netherlands.

The collected sludges were characterized by the differential thermal analysis (DTA) using NETZSCH STA 409 C/CD instrument, in air by 10°C/min, from room temperature to 1100°C. This in term of differential scanning calorimetry (DSC) and thermal gravimetric analysis (TG). FTIR spectra were utilized for detecting the reaction completion, using JASCO FT/IR-6300 type A, recorded in the range of 400-4000 cm^{-1}. The elemental composition of the produced materials was characterized using Thermo Scientific™ K-Alpha™ XPS spectrometer, Al-Kα Micro-focused monochromator within an energy range up to 4 KeV. Zinc aluminate microstructure was investigated by using the scanning electron microscope (SEM) JEOL instrument model JSM-5410, and an accelerating voltage of 20 KV. Samples morphology's information such as particle size and particle shape were investigated using high resolution transmission electron microscopy with an acceleration voltage up to 120 kV, a magnification power up to 600 k, and a resolving power down to 0.2 nm (TEM, JEOL-JEM-1230, Tokyo, Japan). Optical properties of the obtained zinc aluminate samples were studied by using UV-visible absorption spectra and PL emission spectra for band gab measurements. The absorption spectra are recorded JASCO Corp., V-570, Rev. 1.00 spectrometer/data system, in the wavelength ranges from 200 to 1000 nm, at room temperature. The photoluminescence (PL) emission spectra were carried out using a spectrofluorometer (RF-5301 instrument used by spectrum Type EM) at room temperature, by 320 nm excitation wavelength, and scan range from 220-900 nm.

3. Result and discussion

3.1 Industrial wastes characterization

The XRF analysis were carried out for zinc and aluminum sludges, for determining the chemical composition and the weight percentage of all compounds consisting of the sludges. After ignition at 1000°C, XRF analysis show a weight loss reach to 26.6 % and 39.2 % for Zn and Al sludge samples, respectively, Table 1 shows the weight percentage for all the included compounds.

The XRD patterns of zinc and aluminum sludges are illustrated in Fig. 1A and B, respectively. Fig. 1A shows peaks appeared at 2Θ = 13.06°, 24.07°, 25.03°,

28.24°, 31.09°, 32.88°, 33.46°, 35.99°, 38.84°, 43.1°, 47.16°, 53.65°, 58.13° and 60°, they are consistent with the standard card of hydrozincite ($Zn_5(CO_3)_2(OH)_6$) phase (JCPDS, 72-1100) [17]. Fig. 1B shows peaks appeared at 2Θ =18.24°, 20.24°, 32.31°, 33.78°, 36.51°, 36.51°, 37.59°, 39.30°, 40°, 41.59°, 44.14°, 45.35°, 46.1°, 47.29°, 50.54°, 52.17°, 54.28°, 63.73°, 64.53°, 66.11° and 68.81°, they are consistent with the standard card of gibbsite mineral ($Al(OH)_3$) (JCPDS, 70-2038) [18]. XRD spectra of the two sludges don't show any peaks attributed to the other phases appeared in XRF analysis by small traces. This implies that, hydrozincite and gibbsite are the main phases in their sludges.

Table 1 shows the weight percentage of each component in Zn and Al sludges after heating the sludges powders at 1000°C

Compound formula	Zn-sludge (weight %)	Al-sludge (weight %)
Na_2O	---	9.928
MgO	0.132	0.525
Al_2O_3	1.002	48.043
SiO_2	0.976	0.393
P_2O_5	0.051	0.023
SO_3	1.715	0.168
K_2O	0.035	0.021
CaO	2.097	1.087
TiO_2	0.2	0.03
Cr_2O_3	0.008	0.007
MnO	0.273	0.024
Fe_2O_3	3.219	0.450
NiO	---	0.005
CuO	0.017	0.026
ZnO	62.377	0.02
Ga_2O_3	---	0.004
As_2O_3	0.033	---
SrO	0.012	0.017
BaO	0.672	---
PbO	0.334	---
SnO_2	---	0.013
F	0.188	---
Cl	0.062	---

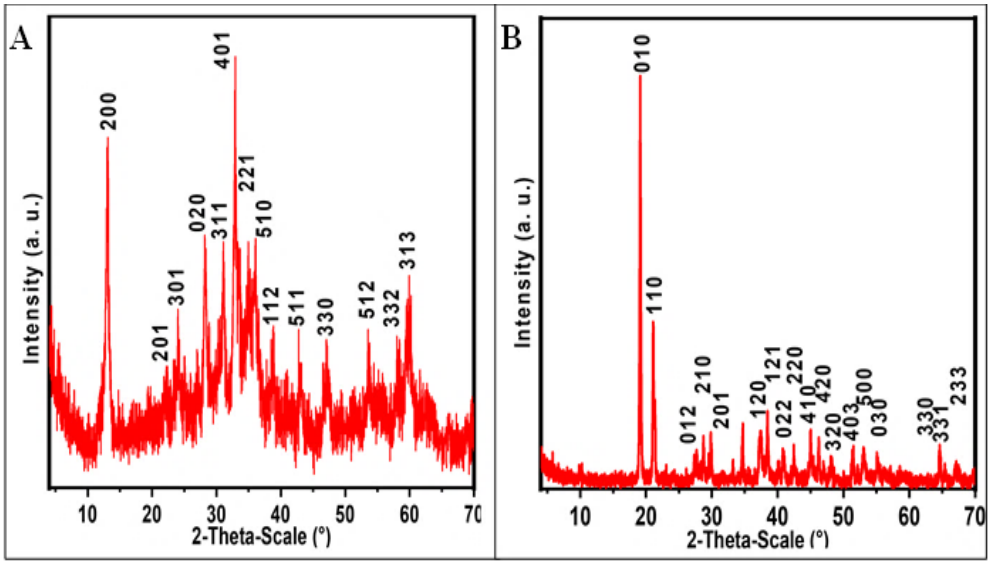

Fig. 1 XRD patterns of zinc (A) and aluminum (B) sludges

Thermal properties of mixture containing hydrozincite ($Zn_5(CO_3)_2(OH)_6$) and gibbsite mineral ($Al(OH)_3$) by 1:2 of Zn: Al were studied by using the differential thermal analysis (DTA). Thermal analysis in term of differential scanning calorimetry (DSC) and thermal gravimetry (TG) curves are shown in Fig. 2A and B, respectively. The DSC curve shows two endothermic peaks (small and sharp) maximized at 134 & 271 °C. The first peak (a small endothermic peak) is attributed to the evaporation of surface adsorbed water molecules. The second peak (a sharp endothermic peak) is related to a fast-thermal decomposition of hydrozincite. This is in line with the literature which found out the decomposition temperature of hydrozincite in temperature range of 240-278°C [19–21], according to the following reaction:

$$Zn_5(CO_3)_2(OH)_6\,(s) \rightarrow 5ZnO\,(s) + 2CO_2\,(g) + 3H_2O\,(g) \quad (1)$$

At the same time, it was found that, the dehydroxylation of gibbsite occurs around 270°C [22,23]. But there are two scenarios previously discussed for the gibbsite transformation process, the first scenario is the direct transformation to aluminum oxide (Al_2O_3) (dehydroxylation) according to reaction 2. The second is indirect one, and this is taking place through the formation of boehmite (AlO(OH)), which per se transforms to aluminum oxide, as given in reactions 3 and 4.

$$2Al(OH)_3\,(s) \rightarrow Al_2O_3\,(s) + 3H_2O\,(g) \quad (2)$$

$$3Al(OH)_3\,(s) \rightarrow Al_2O_3\,(s) + AlO(OH)\,(s) + 4H_2O\,(g) \quad (3)$$

$$2AlO(OH)\,(s) \rightarrow Al_2O_3\,(s) + H_2O\,(g) \quad (4)$$

Boehmite hydroxylation occurs around 500°C according to reaction 3, as discussed in literature. The DSC curve Fig. 2A doesn't show any endothermic peak around this temperature. Consequently, it is clear that gibbsite directly transformed to aluminum oxide according to reaction 2 without passing through the intermediate boehmite formation.

The TG analysis for zinc and aluminum sludges were studied in term of their weight loss or gain during thermal decomposition Fig. 2B. Theoretically, about 28% weight loss was caused by the loss of water and carbon dioxide molecules out from $Zn_5(CO_3)_2(OH)_6$ and $2Al(OH)_3$ thermal decomposition. $Zn_5(CO_3)_2(OH)_6$ (MW= 547 g/mol) loss about 25.95% weight during its decomposition, in the form of two carbon dioxide (88 g) and three water molecules (54 g) according to reaction 1 [20,21]. Additionally, two molecules of $Al(OH)_3$ (MW= 78 g/mol) loss about 34.5% in the form of three water molecules (54 g) from two gibbsite molecules according to reaction 2 [22]. The total weight loss represented in two carbon dioxide and six water molecules (88+54*2=196 g) from the total mixture weight (547+78*2=703). Actually, the TG curve totally reveals ~30% weight loss of the sludge mixture, it was anticipated that, the surface adsorbed water molecules represent 2% up to 134°C. The total weight loss was achieved from the TG curve to align with the theoretical weight loss according to the decomposition reactions. The TG analysis confirms the thermal decomposition of hydrozincite and gibbsite through reactions 1 and 2. Whereas, the extension of the weight loss in the TG curve up to 730°C confirms that, the thermal decomposition of hydrozincite and gibbsite didn't complete at temperature less than this temperature. Finally, it was found that, there isn't any excess weight loss above 730°C and this implies that, sludges' mixture has thermal stability above 730°C owing to the new phase formation.

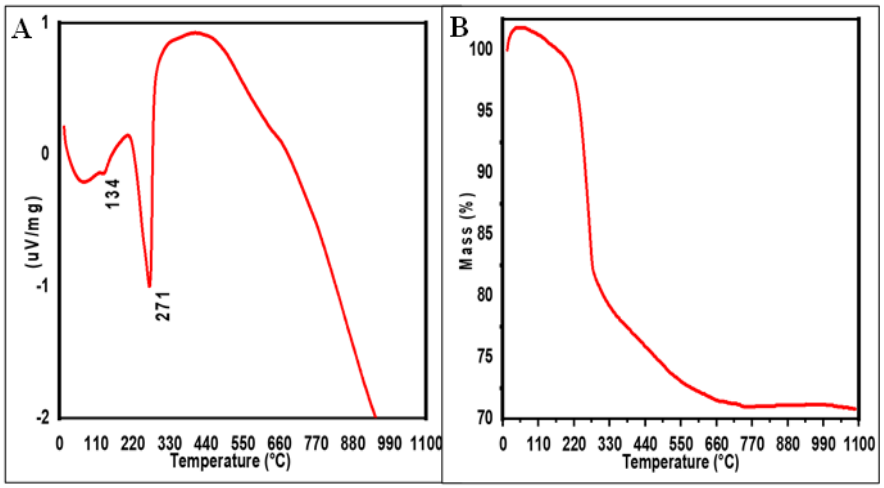

Fig. 2 Differential thermal analysis, DSC (A) and TG (B) of sludges' mixture

3.2 Zinc aluminate characterization

Samples synthesized through SSR and MSS were characterized by XRD analysis for their formation, purity, crystallinity and crystallite size, as shown in Fig. 3. The peaks of the two spectra appeared at 2Θ = 31.26°, 36.79°, 44.87°, 49.08°, 55.63°, 59.28° and 65.25°, they are corresponding to (220), (311), (400), (331), (442), (511) and (440) crystal planes distance, respectively, for zinc aluminate (gahnite) spinel structure (JCPDS, 74-1136) [24]. XRD analysis proved that, pure phase zinc aluminate was achieved by SSR and MSS. The SSR sample spectrum is characterized by higher intensity of peaks than that of MSS sample spectrum, this reveals the high crystallinity of SSR sample. The average crystallite size was calculated by the Debye–Scherrer equation using the most intense peak (311) appeared at 2Θ = 36.79°, it was found to be 17.4 and 12.7 nm for samples synthesized by SSR and MSS, respectively. The broadening of peaks in XRD spectra confirms the nano size of the synthesized samples.

Zinc aluminate formation and purity were examined by FTIR spectra for samples synthesized by SSR and MSS, as shown in Fig. 4. The peaks of the two spectra appeared at 496, 553, 661, 989, 1429, 1646 and 3415 cm^{-1}. The sharp peak appeared at 496 cm^{-1} is a characteristic peak of zinc aluminate and it is attributed to Zn-O-Al, Al-O and Zn-O stretching and bending vibration modes [10,24]. Whereas, the two peaks appeared at 553 and 661 cm^{-1} are attributed to Al-O stretching and O-Al-O bending vibrations of AlO_6 group in spinel type $ZnAl_2O_4$ structure, respectively [24,25]. The small two peaks appeared at 989 and 1429 cm^{-1} are attributed to Al-OH bond bending mode [24], and they are more intense in MSS sample. Finally, the two peaks appeared at 1646 and 3415 cm^{-1} are attributed to O-H bending and stretching vibration modes of adsorbed surface water, respectively [24,25]. FTIR spectra didn't show any impurity peaks for samples synthesized by SSR or MSS, this confirms the XRD result for reaction completion at 1100°C and the formation of single-phase zinc aluminate structure.

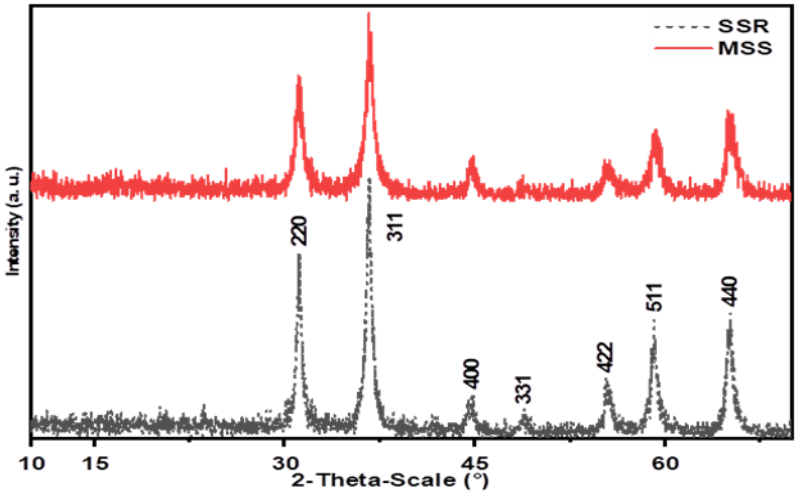

Fig. 3 XRD spectra of zinc aluminate samples synthesized by SSR and MSS

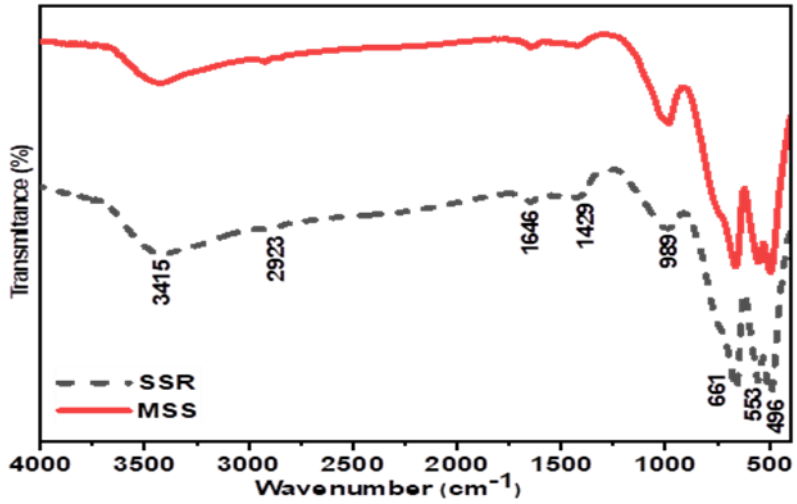

Fig. 4 FTIR spectra of zinc aluminate samples synthesized by SSR and MSS

The elemental composition of zinc aluminate samples synthesized via SSR and MSS was studied by X-ray photoelectron spectroscopy (XPS), as shown in Figs. 5 and 6, respectively. The existence of elements as like as Zn, Al and O were indicated in the full surveys of SSR and MSS samples Fig. 5A and 6A, they have same peaks appeared at 1044.44, 1021.42, 119.08, 978.09, 532.18, 531.22 and 73.56 eV. The two peaks appeared at 1044.44 and 1021.42 eV are corresponding to Zn 2p energy levels in zinc aluminate (illustrated in the high-resolution Fig. 5B and 6B). Single peak appeared at 978.09 eV is corresponding to the carbonate species adsorbed on the surface caused by the calibration for XPS instrument itself. The other two peaks appeared at 532.18 and 531.22 eV are corresponding to the crystalline and adsorbed O 1s energy levels, respectively (illustrated in the high-resolution Fig. 5C and 6C). Whereas, the final two peaks appeared at 119.08 and 73.56 eV are corresponding to Al 2s and Al 2p energy levels (illustrated in the high-resolution Fig. 5D and 6D), respectively [26]. The XPS analysis confirm the reaction completion and proved the formation of $ZnAl_2O_4$ structure, as achieved by XRD and FTIR results.

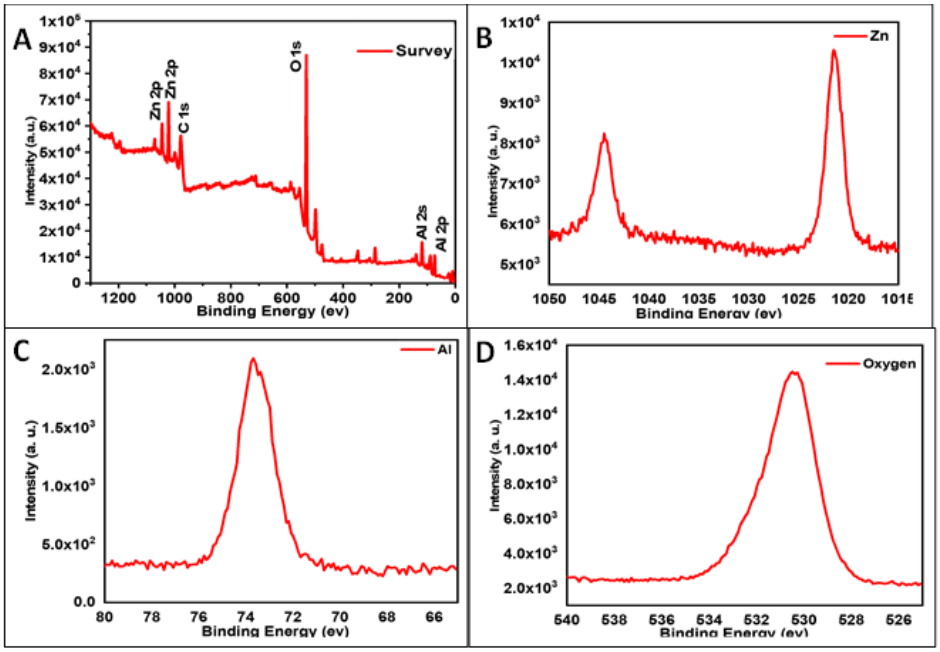

Fig. 5 XPS of zinc aluminate sample synthesized by SSR, A: full survey, B: Zn 2p, C: Al 2p and D: O 1s

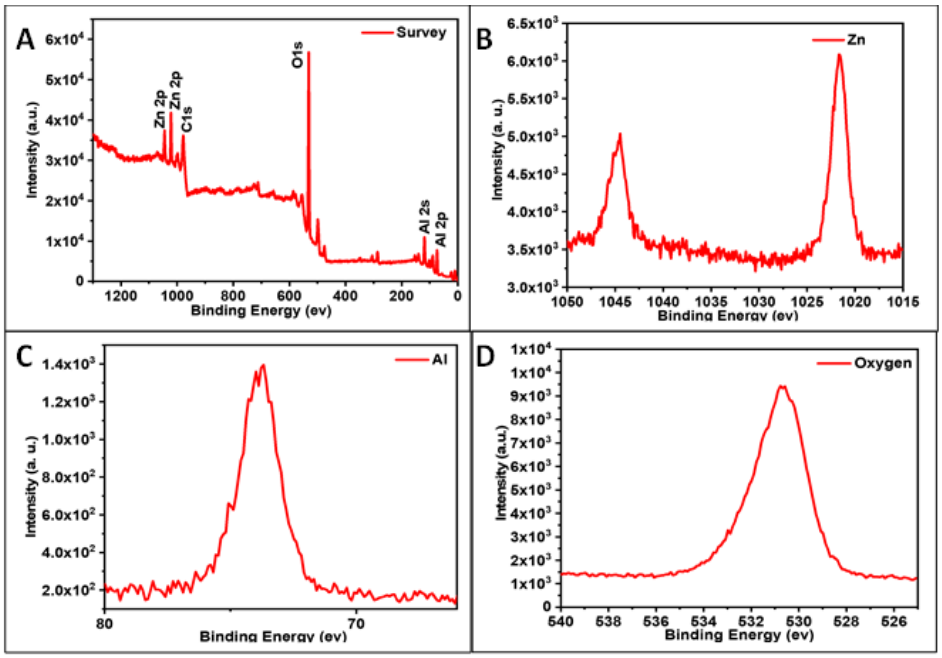

Fig. 6 XPS of zinc aluminate sample synthesized by MSS, A: full survey, B: Zn 2p, C: Al 2p, and D: O 1s

The structure morphology of zinc aluminate samples synthesized via SSR and MSS was studied by using scanning electron microscopy (SEM), as shown in Fig. 7A-D. The microstructure of SSR sample is illustrated in A and B images, whereas, that of MSS sample is illustrated in C and D images. The microstructures consist of plate like particles with a particle size ranging from 10 nm to 1µm, in addition to some large patchy rods appeared in the microstructure of SSR sample. As noticed from images, the microstructure of MSS sample is promoted by structure homogeneity over that of SSR sample. The difference in homogeneity depends on the reaction mechanism in which how the reactants bonded to each other in both routs. There are two probable mechanisms, in the first mechanism aluminum oxide was considered as a spinel surface and zinc oxide as a diffusion ion. Zinc oxide ions penetrate through aluminum oxide surface by vaporization, condensation and surface diffusion process. After covering the aluminum oxide surface by zinc oxide ions, zinc aluminate layer was formed. In the second probable mechanism, zinc and aluminum ions mutually diffuse through a sublattice of oxygen ion, and then bonded together, authors stated that, the second mechanism is more probable in solid state reactions [27].

In case of molten salt synthesis, potassium chloride salt was used as a solvent and large amount is desirable in order to completely dissolve the reactants. MSS reaction mechanism was completed on two stages, the first is called the reaction stage, it occurs in the first few minutes after the supersaturation of the solid solution by the dissolved reactants particles. Molten salt addition enhances the rate of the reaction by increasing the contact area between the reactants particles and achieving high mobility [15,28]. Consequently, the diffusion of zinc oxide to the aluminum oxide lattice in the molten salt media has to be much quicker than in the SSR, proceeding the reaction according to the first mechanism. In this stage, large plate like particles were produced with some surface roughness, which clearly appeared in the high magnification of MSS sample (image F).

The second stage is called the growth stage, in which, the product particles is the lonely solid phase in the molten salt after consuming all the reactants particles in the reaction stage. The growth stage predominantly affected by phenomena which called Ostwald ripening appeared with long time heating [28,29]. In which, large amount of small product particles still dissolved in the molten salt, participate on the surface of large particles, fall in the pores then penetrate in their kink. This phenomenon partially increases the size of large particles and increases their surface roughness. The small particles are dominant in the microstructure of MSS sample, owing to the low degree of aggregation. In which, molten salt covers the particles surface and prevents aggregation of particles which highly occurs in solid state reactions. This responsible for the lower crystallinity of MSS sample appeared in XRD analysis, furthermore, MSS sample was characterized by high structure's homogeneity over SSR sample as observed from SEM investigation, since the produced particles participated from liquid phase.

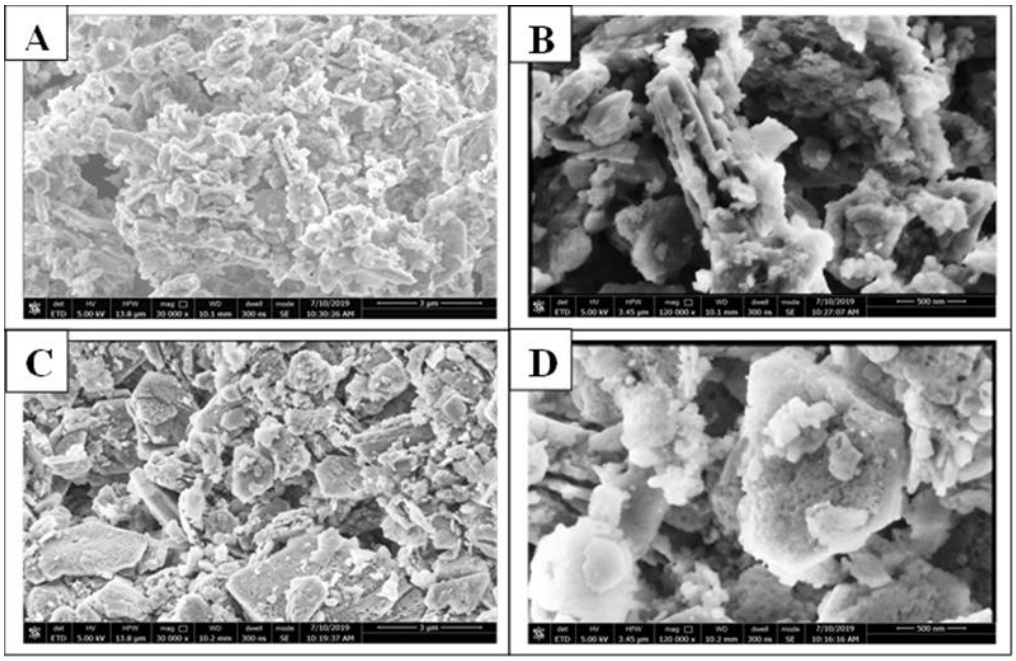

Fig. 7 SEM images of zinc aluminate samples synthesized by SSR (image A, B) and MSS (image C, D)

The high-resolution transmission electron microscopy (HRTEM) was used for investigating more details in the microstructures of zinc aluminate samples synthesized by SSR (Fig. 8A, B, C) and MSS (Fig. 8D, E, F). TEM images confirm that, cubic particles of zinc aluminate were formed by SSR and MSS, and the particles size was found to be ranged from 5 to 100 nm. For SSR sample, the microstructure was characterized by particles aggregation and high crystallinity since, cubic particles could be appeared clearly. For MSS sample, the large plate like particles clearly appeared in image F, whereas, a huge number of very small particles appeared in the high-resolution images D and E. This confirms the reaction mechanism previously discussed in SEM for MSS, in which the particles formed on two stages of liquid-solid reaction. The selective area electron diffraction (SAED) for SSR sample (onset on image C) revealed the appearance of particles with cubic structure, and confirms the high crystallinity by the appearance of obvious light spots. Whereas for MSS sample (onset on image F), SAED image consists of more pronounced cubic structure and light spots. More else, the structure homogeneity was confirmed by the appearance of ordered light spots, in which, the cubic structure was surrounded by light spots in six directions, instead of the slightly confused and messy structure appeared for SSR sample. The high crystallinity of zinc aluminate samples synthesized by SSR and MSS were confirmed in addition to the structure homogeneity for MSS sample over SSR sample.

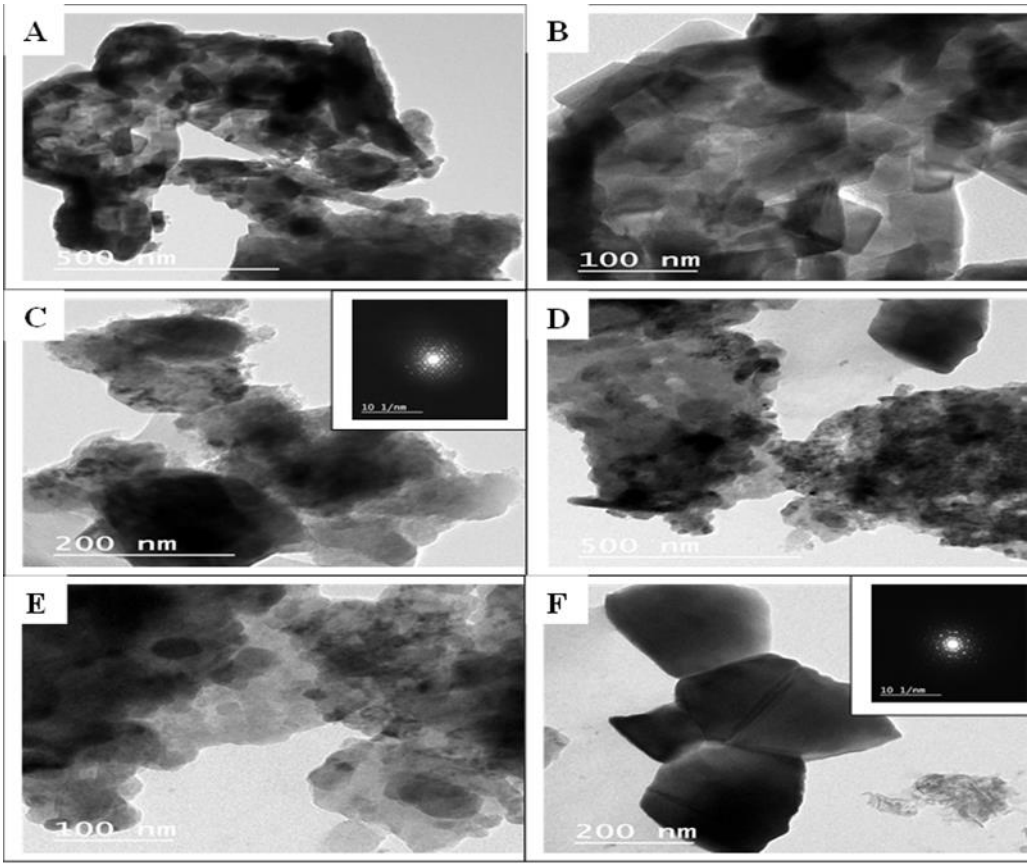

Fig. 8 TEM images of zinc aluminate samples synthesized by SSR (image A, B, C) and MSS (image D, E, F)

Optical properties of zinc aluminate samples synthesized by SSR and MSS were studied using UV-visible absorption spectroscopy, as shown in Figure 9. From Fig. 9A, zinc aluminate samples exhibit one absorption peak appeared at 470 nm and it is consistent for SSR and MSS samples. MSS sample is characterized by high absorbance percentage over SSR sample. The band-gap energy was then determined via constructing a Tauc plot relation between $(\alpha h\nu)^2$ as a function of photon energy $(h\nu)$, where α is the absorbance, as shown in Fig. 9B. The band gab energy was found to be 2.78 and 2.48 eV for SSR and MSS samples, respectively.

Absorbance and band gab energy of nanosize materials

actually depend on several factors, as the crystallinity, particle size, surface roughness and the oxygen deficiency have a significant effect [10]. Whereas, the main reason for the difference in absorbance and the band gab between SSR and MSS samples is the presence of OH-groups of surface adsorbed water molecules by large amounts [30,31]. The FTIR analysis confirms the presence of surface adsorbed water molecules by the appearance of Al-OH bond peaks at 989 and 1429 cm^{-1}, with higher intensity for MSS sample. The scanning electron microscopy investigation illustrated that, the MSS structure morphology greatly influenced by the Ostwald ripening phenomena [28,29]. In which, particles smaller than the critical size dissolved in the molten salt and subsequently precipitated in the kink of the formally formed large particles, creating rough surface. This roughness allows to water molecules to interpret into the surface pores creating oxygen vacancies, which create a localized energy state in zinc aluminate band gab, and decrease the band gab energy over that was found by literature articles (~3-3.9 eV) [29,31–33].

Decreasing the band gab energy may be related to a behavior called mixing of valence band orbitals, which previously observed for zinc aluminate structure. In which, zinc 3d orbital mixed or interfered with 2p orbital of oxygen and this repulses the valence band maximum up to the conduction band reducing the band gab energy to 2.78 eV [34].

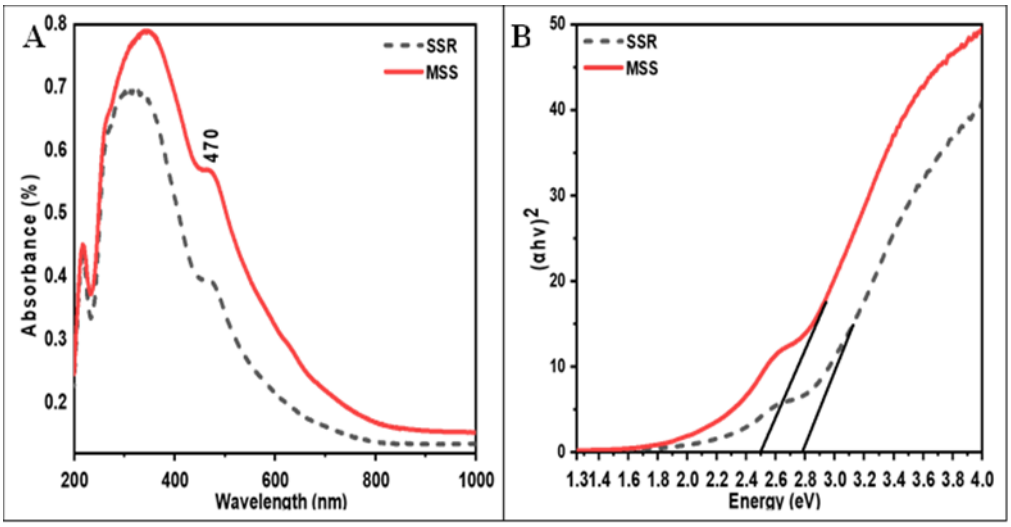

Fig. 9 the UV-visible absorbance (A) and the Tauc plot (B) curves of zinc aluminate samples synthesized by SSR and MSS

Photoluminescence spectroscopy was utilized for studying the emission efficiency of zinc aluminate samples synthesized by SSR and MSS, as shown in Fig. 10. A strong intense peak appeared at 470 nm for the two samples, but with higher intensity for SSR sample. The result obtained by photoluminescence spectroscopy matching well with the band gab value obtained by UV-visible spectroscopy. The difference in intensities of PL spectra between the two samples was corresponding to the difference in crystallinity and the presence of OH-group of surface adsorbed water molecules [35]. Decreasing of OH content enhances the PL emission intensity, meanwhile, the low intensity of the PL peaks is a good indication for the low electron-hole recombination rate, high absorption and high photocatalytic activity [36]. Optical properties obtained by UV-Vis and PL spectroscopy promoted the produced zinc aluminate samples to be used as a photocatalytic material for waste disposal, especially, in waste water treatments.

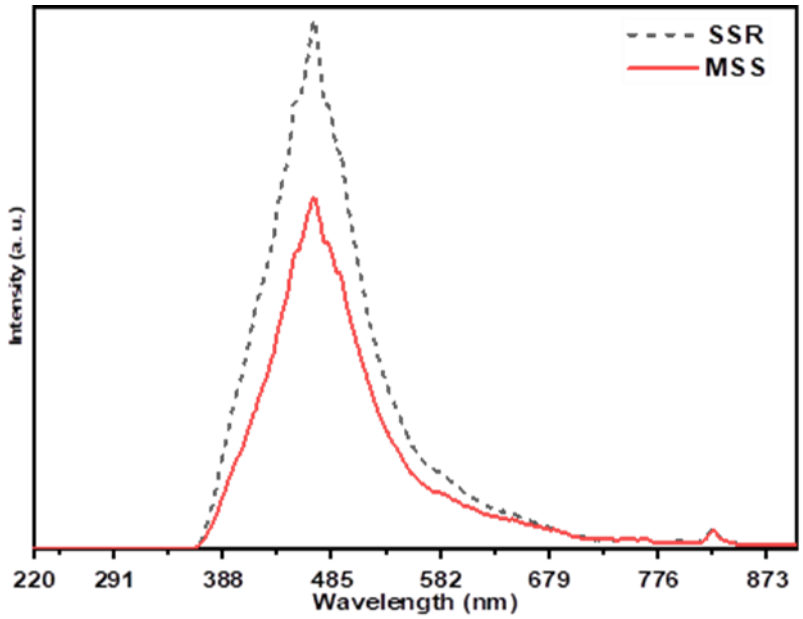

Fig. 10 Photoluminescence emission spectroscopy of zinc aluminate samples synthesized by SSR and MSS

4. Conclusion

Nanosize zinc aluminate powder was synthesized from solid industrial wastes represented in zinc and aluminum sludges. Formally, zinc and aluminum sludges were characterized by XRD, XRF and DTA. The results showed that, zinc and aluminum were found as hydrozincite ($Zn_5(CO_3)_2(OH)_6$) and gibbsite mineral ($Al(OH)_3$) in their sludges, respectively. Thermal analysis of sludges' mixture proved its thermal stability at temperature above 730°C. Secondly, solid-state reaction (SSR) and molten salt synthesis (MSS) were performed at the same conditions of 1100°C for 5 h by 3°C/min, using potassium chloride (KCl) as a molten salt. The structural properties of the produced samples were characterized by XRD, FTIR and XPS analysis and the results showed that, pure phase zinc aluminate nanoparticles were formed. The structure morphology of the synthesized samples was studied by the SEM, the microstructure of MSS sample was characterized by a structure homogeneity over that of SSR. The high-resolution TEM confirms the SEM result and expressed more details related to the particles growth according to a definite mechanism for both SSR and MSS routs. SSR and MSS samples were investigated by using UV-visible and PL spectroscopy in term of their absorbance efficiency and band gab, samples proved excellent optical properties promoting them for photocatalytic applications as dyes removal from waste water.

5. Conflict of Interest

The authors declare that there are no conflicts of interest regarding the publication of this paper.

6. References

1. **Pinto, V. S., Luz, A. P., Borges, O. H. and Pandolfelli, V. C. (2022).** Binder effect on $ZnAl_2O_4$-containing high-alumina refractory castables. Ceram. Int., **48:** 11401 – 11409. https://doi.org/10.1016/j.ceramint.2021.12.363.
2. **Shaban, M., Hosny, R., Rabie, A. M., Shim, J. J., Ahmed, S. A., Betiha, M. A. and Negm, N. A. (2020).** Zinc aluminate nanoparticles: Preparation, characterization and application as efficient and economic catalyst in transformation of waste cooking oil into biodiesel. J. Mol. Liq., **302:** 112377. https://doi.org/10.1016/j.molliq.2019.112377

3. **Pipattanaporn, P., Pansiri, P., Kumpeerakij, P., Yaemphutchong, S., Siri-apai, P., Suetrong, N., Chansaenpak, K., Singkammo, S., Kanjanaboos, P., Hanlumyuang, Y., Wannapaiboon, S. and Wattanathana, W. (2022).** Effect of triethanolamine chelating agent on crystallinities, phase purities, and optical properties of zinc aluminate spinel synthesized by thermal decomposition. Ceram. Int., **48:** 8186 – 8195. https://doi.org/10.1016/j.ceramint.2021.12.021.
4. **Battiston, S., Rigo, C., Da Cruz Severo, E., Mazutti, M. A., Kuhn, R. C., Gündel, A. and Foletto, E. L. (2014).** Synthesis of zinc aluminate ($ZnAl_2O_4$) Spinel and its application as photocatalyst. Mater. Res., **17:** 734 – 738. https://doi.org/10.1590/S1516-14392014005000073.
5. **Siragam, S., Dubey, R. S., Pappula, L. and Satheesh Babu, G., (2022).** Synthesis and investigation of dielectric ceramic nanoparticles for microstrip patch antenna applications. Sci. Rep., **12:** 1 – 10. https://doi.org/10.1038/s41598-022-07899-6.
6. **Venkatesh, R., Yadav, L. S. R. and Dhananjaya, N. (2021).** Rare earth activated bio synthesis of zinc aluminate for photocatalytic activity of dye. Mater. Today Proc., **49:** 628 – 631. https://doi.org/10.1016/j.matpr.2021.04.534.
7. **Baiju, V., Devadathan, D. and Sajeevkumar, G. (2021).** Photocatalytic degradation of toxic organic pollutants using zinc aluminate nanocomposite. Mater. Today Proc., 47: 1507–1513. https://doi.org/10.1016/j.matpr.2021.06.066.
8. **Putra, A. T. S. P. (2020).** An improved method for high photocatalytic performance of $ZnAl_2O_4$ spinel derived from layered double hydroxide precursor. SN Appl. Sci., **2:** 1 – 10. https://doi.org/10.1007/s42452-020-2682-7.
9. **Sotelo Martin, L. E. and Castro, R. H. R. (2022).** Al excess extends Hall-Petch relation in nanocrystalline zinc aluminate. J. Am. Ceram. Soc., **105:** 1417 – 1427. https://doi.org/10.1111/jace.18176.
10. **Rahman, A., Charoo, M. S. and Jayaganthan, R. (2015).** Structural, optical and photocatalytic properties of zinc aluminate spinel nanoparticles. Mater. Technol., **30:** 168 – 176. https://doi.org/10.1179/1753555714Y.0000000211.
11. **Baiju, V., Devadathan, D., Rejani, P., Sajeevkumar, G. and Raveendran, R. (2021).** Effect of annealing temperature in the purity of zinc aluminate synthesized by solution combustion method. AIP Conf. Proc., **2379:** 1-5. https://doi.org/10.1063/5.0058365.
12. **Siragam, S., Dubey, R. S. and Pappula, L. (2021).** Investigation of structural, chemical, morphological and dielectric properties of sol-gel derived $ZnAl_2O_4$ nanoparticles. Mater. Today Proc., **45:** 2091 – 2095. https://doi.org/10.1016/j.matpr.2020.09.629
13. **Wei, X. and Chen, D. (2006).** Synthesis and characterization of nanosized zinc aluminate spinel by sol-gel technique. Mater. Lett., **60:** 823 – 827. https://doi.org/10.1016/j.matlet.2005.10.024.
14. **Li, Z., Zhang, S. and Lee, W. E. (2007).** Molten salt synthesis of zinc aluminate powder. J. Eur. Ceram. Soc., **27:** 3407 – 3412. https://doi.org/10.1016/j.jeurceramsoc.2007.02.195.
15. **Sikalidis, C. (2012).** Advances in Ceramics - Synthesis and Characterization, Processing and Specific Applications. https://doi.org/10.5772/985.
16. **Vereš, J., Jakabský, Š. and Lovás, M. (2011).** Zinc recovery from iron and steel making wastes by conventional and microwave assisted leaching. Acta Montan. Slovaca., **16:** 185 – 191.
17. **Carbone, M., Briancesco, R. and Bonadonna, L. (2017).** Antimicrobial power of Cu/Zn mixed oxide nanoparticles to Escherichia coli. Environ. Nanotechnology, Monit. Manag., **7:** 97 – 102. https://doi.org/10.1016/j.enmm.2017.01.005.
18. **Arogundade, A. I., Ahmad, F., Bhat, A. H., Gillani, Q. F. and Megat-Yusoff , P. S. M. B. (2016).** Investigating the Synergistic Effect of Bauxsol™ in an Epoxy Intumescent Coating System. Procedia Eng., **148:** 223 – 227. https://doi.org/10.1016/j.proeng.2016.06.579.

19. **Zhan, Q. W. and Qian, C. X. (2016).** Microbial-induced synthesis of nanoparticles of zinc phosphate and basic zinc carbonate based on the degradation of glyphosate. Dig. J. Nanomater. Biostructures., **11:** 393 – 399.
20. **Kanari, N., Mishra, D., Gaballah, I. and Dupré, B. (2004).** Thermal decomposition of zinc carbonate hydroxide. Thermochim. Acta. Elsevier., **410:** 93 –100.
21. **Haq, I. U. and Azad, A. M. (2012).** Experimental artifacts for morphological tweaking of chemical sensor materials: Studies on ZnO. Sensors (Switzerland), **12:** 8259 – 8277. https://doi.org/10.3390/s120608259.
22. **Earnest, C. M., Karla, G. and Britney, S. (2018).** Improved Quantification of Gibbsite in Bauxite Ores by Thermogravimetric Methods (TGA and DTG). Adv. Appl. Chem. Biochem., **1:** 9 – 17. https://doi.org/10.33513/arms/1801-02.
23. **Kloprogge, J. T., Ruan, H. D. and Frost, R. L. (2002).** Thermal decomposition of bauxite minerals: Infrared emission spectroscopy of gibbsite, boehmite and diaspore. J. Mater. Sci**., 37:** 1121 – 1129. https://doi.org/10.1023/A:1014303119055.
24. **Abd El All, S., Fawzy, Y. H. A. and Radwan, R.M. (2007).** Study on the structure and electrical behaviour of zinc aluminate ceramics irradiated with gamma radiation. J. Phys. D. Appl. Phys., **40**: 5707 – 5713. https://doi.org/10.1088/0022-3727/40/18/029.
25. **Sunder, S., Rohilla, S., Kumar, S. and Aghamkar, P. (2011).** Structural characterization of spinel zinc aluminate nanoparticles prepared by coprecipitation method. AIP Conf. Proc., **1393:** 123 – 124. https://doi.org/10.1063/1.3653640.
26. **Strohmeier, B. R. (1994).** Zinc Aluminate ($ZnAl_2O_4$) by XPS. Surf. Sci. Spectra., **3:** 128 – 134. https://doi.org/10.1116/1.1247773.
27. **Nagata, K., Sato, K. and Goto, K.S. (1980).** Kinetics of the solid state reaction between zinc oxide and aluminum oxide. Metall. Trans. B., **11:** 455 – 461. https://doi.org/10.1007/BF02676889.
28. **Mohamed N. R. (1996).** Ceramic processing and sintering**.**
29. **Chen, X. Y., Ma, C., Zhang, Z. J. and Wang, B.N. (2008).** Ultrafine gahnite ($ZnAl_2O_4$) nanocrystals: Hydrothermal synthesis and photoluminescent properties. Mater. Sci. Eng. B Solid-State Mater. Adv. Technol., **151:** 224 – 230. https://doi.org/10.1016/j.mseb.2008.09.023.
30. **Khan, M. M., Ansari, S. A., Pradhan, D., Han, D. H., Lee, J. and Cho, M. H. (2014).** Defect-induced band gap narrowed CeO_2 nanostructures for visible light activities. Ind. Eng. Chem. Res., **53:** 9754 – 9763. https://doi.org/10.1021/ie500986n.
31. **Sumathi, S. and Kavipriya, A. (2017).** Structural, optical and photocatalytic activity of cerium doped zinc aluminate. Solid State Sci., **65:** 52 – 60. https://doi.org/10.1016/j.solidstatesciences.2017.01.003.
32. **Wang, S. F., Sun, G. Z., Fang, L. M., Lei, L., Xiang, X. and Zu, X. T. (2015).** A comparative study of $ZnAl_2O_4$ nanoparticles synthesized from different aluminum salts for use as fluorescence materials. Sci. Rep., **5:** 1 – 12. https://doi.org/10.1038/srep12849.
33. **Mathur, S., Veith, M., Haas, M., Shen, H., Lecerf, N., Huch, V., Hüfner, S., Haberkorn, R., Beck, H. P. and Jilavi, M. (2004).** Single-Source Sol-Gel Synthesis of Nanocrystalline $ZnAl_2O_4$: Structural and Optical Properties. J. Am. Ceram. Soc., **84:** 1921 – 1928. https://doi.org/10.1111/j.1151-2916.2001.tb00938.x.
34. **Sampath, S. K., Kanhere, D. G. and Pandey, R. (1999).** Electronic structure of spinel oxides: Zinc aluminate and zinc gallate. J. Phys. Condens. Matter., **11:** 3635 – 3644. ttps://doi.org/10.1088/0953-8984/11/18/301.
35. **Tsai, M. T., Chang, Y. S., Huang, I. B. and Pan, B. Y. (2013).** Luminescent and structural properties of manganese-doped zinc aluminate spinel nanocrystals. Ceram. Int., **39:** 3691 – 3697. https://doi.org/10.1016/j.ceramint.2012.10.201.
36. **Yang, S. F., Niu, C. G., Huang, D. W., Zhang, H., Liang, C. and Zeng, G. M. (2017).** $SrTiO_3$ nanocubes decorated with Ag/AgCl nanoparticles as photocatalysts with enhanced visible-light photocatalytic activity towards the degradation of dyes, phenol and bisphenol A. Environ. Sci. Nano., **4**: 585 – 595. https://doi.org/10.1039/c6en00597g.